Journal of Microscopy

Journal of Microscopy, Vol. 00, Issue 00 2020, pp. 1–9
Received 31 August 2019; accepted 8 May 2020

doi: 10.1111/jmi.12901

Multislice image simulations of sheared needle-like precipitates in an Al-Mg-Si alloy

E. CHRISTIANSEN*,†, I. G. RINGDALEN‡, R. BJØRGE‡, C. D. MARIOARA*,‡ & R. HOLMESTAD*,†

*Centre for Advanced Structural Analysis (CASA), NTNU – Norwegian University of Science and Technology, Trondheim, Norway
†Department of Physics, Faculty of Natural Sciences, NTNU, Høgskoleringen 5, Trondheim, 4791, Norway
‡Materials and Nanotechnology, SINTEF Industry, Trondheim, 7465, Norway

Key words. Aluminium alloys, Deformation, High resolution transmission electron microscopy, Multislice simulations, Scanning transmission electron microscopy, Transmission electron microscopy.

Summary

The image contrast of sheared needle-like β'' precipitates in the Al-Mg-Si alloy system is investigated with respect to shear-plane positions, the number of shear-planes, and the active matrix slip systems through multislice transmission electron microscopy image simulations and the frozen phonon approximation. It is found that annular dark field scanning transmission electron microscopy (ADF STEM) images are mostly affected by shear-planes within a distance $\sim$ 6–18 unit cells from the specimen surface, whereas about 5–10 equidistant shear-planes are required to produce clear differences in HRTEM images. The contrast of the images is affected by the Burgers vector of the slip, but not the slip plane. The simulation results are discussed and compared to experimental data.

Introduction

Zone axis annular dark field (ADF) scanning transmission electron microscopy (STEM) is a focus-sensitive Z-contrast imaging technique that is very sensitive to the initial part of the specimen (Pennycook & Jesson, 1991; Hillyard & Silcox, 1993; Hillyard *et al.*, 1993; Klenov & Stemmer, 2006; Martinez *et al.*, 2018), whereas zone axis high-resolution transmission electron microscopy (HRTEM) is a thickness-sensitive technique that contains information about the entire projected crystal potential (Cowley & Moodie, 1957; Van Dyck & Chen, 1999; Van Aert *et al.*, 2007; Xu *et al.*, 2010). Images of crystals with through-thickness variation in structure and/or composition are therefore challenging to interpret, and image simulations are required to understand the effect such variations has on the final images. In this work, frozen phonon multislice image simulations are used to investigate the contrast in images of sheared needle-like β'' precipitates (Poole *et al.*, 2005; Misumi *et al.*, 2014; Christiansen *et al.*, 2019b) in the age-hardenable Al-Mg-Si alloy system.

When a coherent or semicoherent precipitate is sheared by a dislocation, a number of crystal defects may form both in the precipitate phase and in the surrounding matrix, or at the interface. Such defects include dislocation loops, interface steps and local crystalline disorder (Ardell, 1985). The strengthening contribution of the precipitate phase will depend on which of these defects are formed, and thus will depend on the crystal structure of the precipitate, the active slip system and the distribution of slip. Transmission electron microscopy (TEM) can be used to investigate the defects after they have formed, and is an important tool for gaining more knowledge of these industrially important alloys. Hence, it is also important to understand how TEM images of sheared precipitates may appear in various cases. In this work, we investigate three cases:

(A) How the distance from the specimen surface to the first shear-plane affects ADF STEM images.
(B) How the number of shear-planes influence HRTEM images.
(C) How different slip systems affect the final images.

The goal of this study is not to answer questions regarding the physical processes of β'' shearing directly, but rather to understand how certain aspects of sheared precipitates affect the image forming processes.

The three case studies are motivated by the incompatibility between the Al matrix slip systems, $\langle 1\bar{1}0\rangle_{\mathrm{Al}}/\{111\}_{\mathrm{Al}}$, and the β'' precipitate crystal structure. Because the β'' precipitate crystal phase usually has a monoclinic unit cell with $a = 15.16$ Å, $b = 4.05$ Å, $c = 6.74$ Å and $\beta = 105.3°$ (Edwards *et al.*, 1998; Andersen *et al.*, 1998; Saito *et al.*, 2018), the matrix slip systems are not valid for the precipitate and

Correspondence to: E. Christiansen, Centre for Advanced Structural Analysis (CASA), NTNU - Norwegian University of Science and Technology, Trondheim, N–7491, Norway. Tel: +4773594628; e-mail: emil.christiansen@ntnu.no

© 2020 The Authors. *Journal of Microscopy* published by John Wiley & Sons Ltd on behalf of Royal Microscopical Society

This is an open access article under the terms of the Creative Commons Attribution License, which permits use, distribution and reproduction in any medium, provided the original work is properly cited.

Table 1. Approximate equivalent lattice planes and directions between Al and variants of β'' with corresponding deviation angles $\Delta\theta$.

	Al	β_A"	$\Delta\theta$ [°]	β_B"	$\Delta\theta$ [°]
Planes	(111)	$(1\,1\,2)$	1.4	$(\bar{1}\,1\,2)$	4.6
	$(\bar{1}11)$	$(5\,1\,\bar{1})$	1.1	$(5\,1\,0)$	3.3
	$(1\bar{1}1)$	$(\bar{5}\,1\,1)$	1.1	$(\bar{5}\,1\,0)$	3.3
	$(11\bar{1})$	$(1\,\bar{1}\,2)$	1.4	$(\bar{1}\,\bar{1}\,2)$	4.6
Directions	$\frac{1}{2}[110]$	$[\frac{1}{11}\,0\,\frac{1}{2}]$	2.7	$[\frac{1}{74}\,0\,\frac{1}{2}]$	0.5
	$\frac{1}{2}[011]$	$[\frac{1}{8}\,\frac{1}{2}\,\frac{1}{6}]$	1.4	$[\frac{1}{10}\,\frac{1}{2}\,\frac{1}{4}]$	1.1
	$\frac{1}{2}[101]$	$[\frac{-1}{23}\,\frac{1}{2}\,\frac{1}{4}]$	0.9	$[\frac{-1}{11}\,\frac{1}{2}\,\frac{1}{6}]$	0.7
	$\frac{1}{2}[\bar{1}10]$	$[\frac{1}{6}\,0\,\frac{-1}{12}]$	0.1	$[\frac{1}{5}\,0\,\frac{1}{12}]$	0.7
	$\frac{1}{2}[0\bar{1}1]$	$[\frac{-1}{8}\,\frac{1}{2}\,\frac{-1}{6}]$	1.4	$[\frac{-1}{10}\,\frac{1}{2}\,\frac{-1}{4}]$	1.1
	$\frac{1}{2}[10\bar{1}]$	$[\frac{-1}{23}\,\frac{-1}{2}\,\frac{1}{4}]$	0.9	$[\frac{-1}{11}\,\frac{-1}{2}\,\frac{1}{6}]$	0.7

the precipitate crystal structure must change locally when sheared. The semicoherency of the precipitate phase makes the precipitates appear as long needles along ⟨100⟩ with $(001)_{\mathrm{Al}} \parallel (010)_{\beta''}$, $[310]_{\mathrm{Al}} \parallel [001]_{\beta''}$ and $[\bar{2}30]_{\mathrm{Al}} \parallel [100]_{\beta''}$ (Edwards *et al.*, 1998; Andersen *et al.*, 1998; Saito *et al.*, 2018). This orientation relationship gives two different orientations of the precipitate phase, β''_A and β''_B. β''_A is oriented according to the previous orientation relationship, and β''_B is oriented with $[\bar{3}20]_{\mathrm{Al}} \parallel [100]_{\beta''}$. From these orientation relationships, it is possible to calculate approximate lattice planes and directions in the precipitate phase that correspond to the matrix slip systems, as shown in Table 1. It is clear that the different matrix slip systems will produce different sheared precipitate structures, and it is therefore interesting to investigate how these different structures will appear when imaged by ADF STEM and HRTEM. In principle, such investigations may enable future experimental work to establish whether precipitates are more easily sheared on some slip systems than others.

Methods

Models of rigidly displaced β'' segments in a matrix of aluminium were prepared using a combination of density functional theory and molecular dynamics. The precipitate structure and size were set up using bulk values for β'' calculated from density functional theory (Ninive *et al.*, 2014). Several atomistic models with different shearing configurations were prepared by rigidly shifting the precipitate accordingly, and subsequently relaxing the surrounding matrix (but keeping the precipitate fixed) using molecular dynamics with LAMMPS (Plimpton, 1995) and the Al-Mg potential by Liu & Adams (1998). Precipitates are rigidly sheared on n planes by N Burgers vector shifts on a given matrix slip system in different configurations. One of the models are shown in Figure 1. HRTEM images are simulated for the complete model (with a bandwidth of 2/3 to reduce aliasing effects). When presented however, the HRTEM images have been cropped to aid readability. Subregions of the models are used for STEM simulations in order to reduce calculation time.

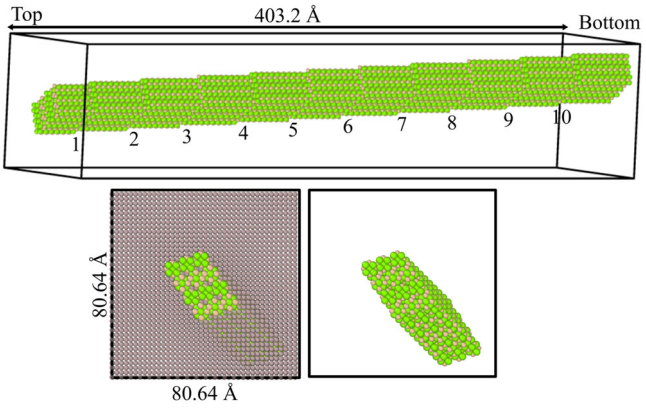

Fig. 1. One of the models used in the study. The β'' precipitate embedded in an aluminium matrix has been sheared n times on a certain slip system at regular intervals (in this case, $n = 10$ and the slip system is $\frac{a}{2}[1\bar{1}0]/(001)_{\mathrm{Al}}$). The visualization was performed with the open visualization tool OVITO (Stukowski, 2010). Al atoms are shown in transparent grey, Mg in green and Si in brown.

Table 2. Multislice simulation parameters.

Parameter	Value	
Acceleration voltage	200 kV	
Detector response	homogeneous	
Potential sampling	2048 × 2048	
Model size	80.64 × 80.64 Å^2	
Model thickness	403.2 Å	
Slice thickness	2.025 Å	
Temperature	300 K	
Number of phonon configurations	20	
	STEM	HRTEM
Convergence semi-angle	27 mrad	–
Defocus C_1	0 nm	−57 nm
Spherical aberration C_3	−300 nm	1.0 mm
Inner collection semi-angle	48 mrad	–
Outer collection semi-angle	206 mrad	–
Image pixel size	0.162 Å	0.039 Å

Frozen phonon multislice simulations were carried out using the MULTEM software and the scattering potentials by Lobato *et al.* (Lobato & Van Dyck, 2014, 2015; Lobato *et al.*, 2016). Due to the nature of the problem, relatively large models are required, which calls for fast and efficient computing. Simulations were therefore performed on a cluster using *NVIDIA TESLA P-100* GPUs (Själander *et al.*, 2019). Large models are required in order to fit a precipitate of reasonable size and to prevent the sheared segments from interfering with each other due to the inherent periodicity in the x–y plane of the simulations. HRTEM and ADF STEM simulations were carried out using the parameters shown in Table 2 and

with Debye–Waller factors for Al, Mg and Si from Peng *et al.* (1996). The simulation parameters are similar to corresponding experimental values used in Christiansen *et al.* (2019b). In addition to the ADF angular interval, bright field and high-angle ADF intervals (0–40 mrad and 100–206 mrad, respectively) were also used to validate the results. The ADF images appeared qualitatively similar to simulated high-angle ADF images, indicating that the ADF collection interval produces images with sufficiently incoherent contrast. Spatial and temporal incoherency are neglected in the STEM simulations, but ADF STEM images are filtered with a Gaussian kernel (1 Å full width at half maximum) to approximate the effect of source incoherency. The effective source size was not measured experimentally, but adjusted to fit experimental images and lies within a reasonable source size range (Maunders *et al.* 2011; Kirkland, 2010). For the HRTEM simulations, a spatial incoherence of 0.0072 $Å^{-1}$ was used. The present study is limited to a qualitative comparison between experimental and simulated images, as quantitative comparisons are considered challenging due to the large number of possible permutations of shear configurations. However, singular value decomposition by robust principal component analysis (Zhou & Tao, 2011) and blind source separation (Hyvärinen & Oja, 2000) routines are used through the HyperSpy (de la Peña *et al.*, 2019) python package to perform a more statistically based analysis of the through-thickness development of fast Fourier transform (FFT) power spectra of HRTEM results.

Results and discussion

A – The effect of shear-plane position on ADF STEM images

The first task is to investigate the depth-sensitivity of ADF STEM in order to understand the range of shear plane depths that give observable contrast. To answer this, we have performed multislice image simulations of models with a single shear-plane at a certain distance z below the surface. For simplicity, the shear-plane was chosen parallel to the specimen surface as $(001)_{\mathrm{Al}}$. Figure 2 shows simulated ADF STEM images where the z position of the shear-plane is varied. For shear-planes close to the specimen surface ($z \sim 6$ unit cells), the beam is able to channel along the atomic columns of the second segment and the final STEM image shows the β'' unit cell of this lower segment rather than the first segment. For intermediate distances ($z \sim 12$ unit cells) from the surface, the image appears like a superposition of the displaced crystal structures. Finally, for greater distances ($z \sim 18$ unit cells and more), the ADF STEM image is dominated by the signal from the initial segment. This means that only shear-planes within a range $\sim$ 6–18 unit cells below the surface will affect ADF STEM images. If more shear-planes occur further down, this may of course reduce channelling and reduce the contrast of the final image further, but the atomic columns are unlikely to be resolved. This is briefly investigated further in later sections.

B – The effect of the number of shear-planes on HRTEM images

For investigating how precipitates with several shear-planes may appear in HRTEM, we have performed HRTEM image simulations of atomistic models with various numbers of shear-planes through the thickness. In principle, the z-position of the shear-planes should also be investigated as in the previous section, but this gives too many variables to cover in the present work. We will therefore limit ourselves to models with near-equidistant shear-planes. This also means that, because of the contrast reversals of HRTEM images, the direct contrast in the simulation results are somewhat arbitrary. However, the FFTs of the images should reveal how various β'' spatial frequencies are transferred for different numbers of shear-planes. Figure 3 presents HRTEM images of models with 5 and 10 shear-planes distributed along the needle axis, along with HRTEM FFT power spectra. With fewer than five shear-planes, no marked change occurred in the fast FFT power spectra of the HRTEM images and are therefore not shown. It is clear that some expected precipitate frequencies of sheared models are transferred whereas others are not. Frequencies in bands perpendicular to the Burgers vector ($[1\bar{1}0]_{\mathrm{Al}}$ in this case) that pass through $\{110\}_{\mathrm{Al}}$ frequencies are transferred, leaving frequencies in-between these bands weak. For instance, this makes the $(20l)_{\beta''}$ and $(40\bar{l})_{\beta''}$ frequency components remain, whereas the $(20\bar{l})_{\beta''}$ and $(40l)_{\beta''}$ frequencies are weakened. The orientation of the band of weak frequencies indicates that the weakening is related to the active slip system. In the next section, this is investigated further, along with the effect of active slip systems on ADF STEM simulations. Before investigating the different slip systems however, the through-thickness development of the band-like weakening of Fourier components is discussed.

Closer inspection of how the images evolve through the thickness (not shown, but data and plots are provided in Christiansen *et al.*, 2020) reveals that the frequency components start to weaken about half-way through the specimen, i.e. after about four or five shearing events. The through-thickness stacks of FFT power spectra were separated into 11 principal components by principal component analysis (Zhou & Tao, 2011) and the two major components were subsequently separated by singular value decomposition through blind source separation (Hyvärinen & Oja, 2000). This analysis, available through Christiansen *et al.* (2020), shows that the FFT power spectra of unsheared precipitates are quite well-described by one component representing the β'' frequency components, and a component of ring-like FFT-features. For sheared precipitates, one of the independent components is a mix of the perfect β'' FFT power spectrum and the ring-like FFT-features, and starts out with a significant contribution to the total signal but decreases steadily until it settles to a relatively constant contribution after half the thickness. This decrease coincides with an increase in the other independent component, which relates to the band-like weakening of precipitate frequencies seen in

© 2020 The Authors. *Journal of Microscopy* published by John Wiley & Sons Ltd on behalf of Royal Microscopical Society,

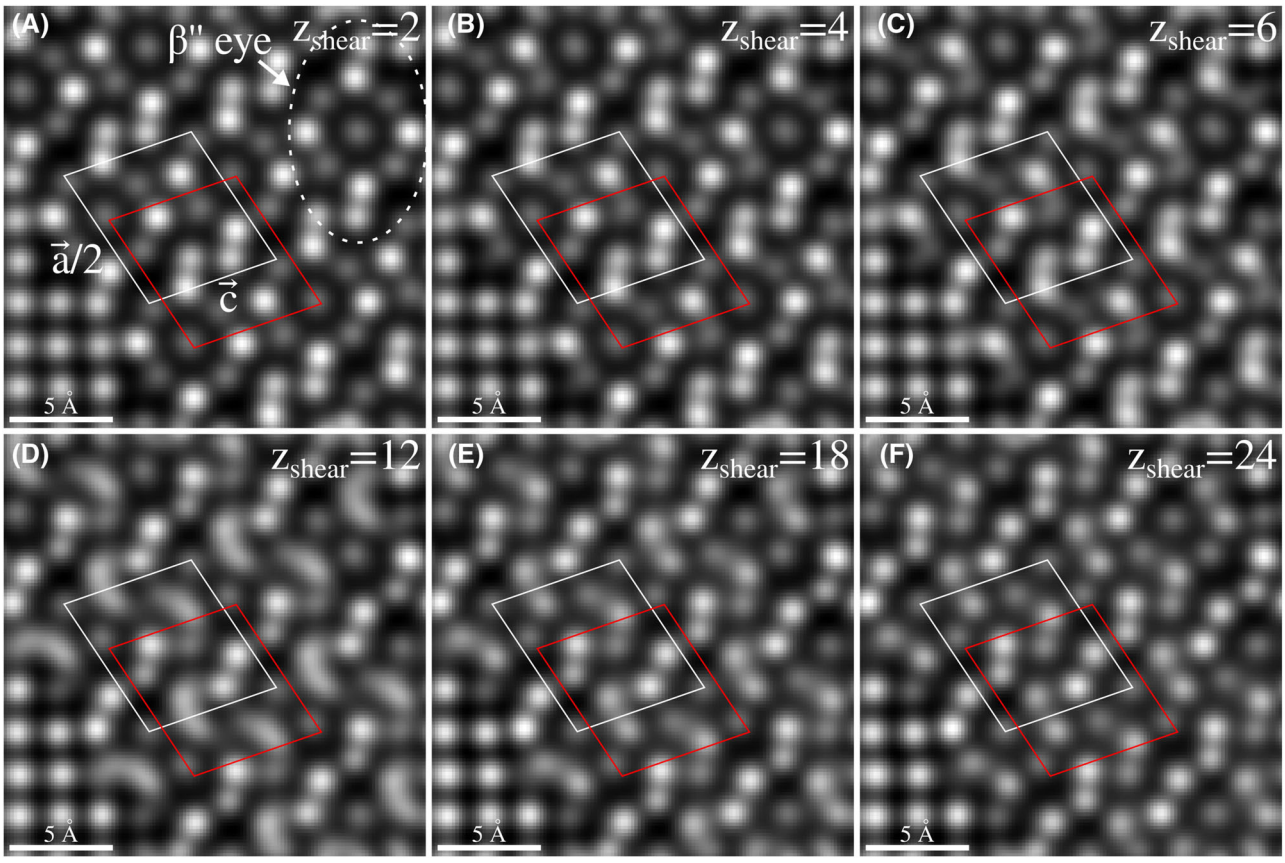

Fig. 2. The effect of the z-position of a single $[1\bar{1}0]_{Al}$ shear-plane in a β'' precipitate in an aluminium matrix on ADF STEM image formation. ADF STEM images of models with a shear-plane at 2, 4, 6, 12, 18, and 24 unit cells below the specimen surface are shown in A to F, respectively, and is indicated by the number in the top-right corners of each image. White and red boxes indicate location of the β'' half-unit cells above and below the shearing planes, respectively, with the corners corresponding to the centres of the β'' 'eyes'.

the final images. The statistical analysis of the through-stack evolution of the FFT power spectra of HRTEM images therefore shows that each shear-plane contributes to the band-like weakening of β'' frequency components. It also shows that five to six shear-planes are sufficient to develop this band-like appearance, as the independent components increased in the first half of the specimen and saturated after five to six shear-planes. Although blind source separation of principal components of a dataset should be interpreted with care, this statistical measure provides more support for our results and interpretations and offers an alternative to the qualitative interpretation in the previous section.

C – The effect of slip systems on ADF STEM and HRTEM images

The effect of various slip systems should produce different atomic column arrangements, and we have performed multislice simulations of precipitates that have been sheared on different slip systems to investigate their effect on ADF STEM and HRTEM images. Because shear-planes only have a significant effect on HRTEM images if there are enough of them, and ADF STEM images are only sensitive to shear-planes close to the specimen surfaces, we show only results of models with 10 shear-planes here as these satisfy both conditions. Furthermore, we have investigated both $(111)_{Al}$ and $(001)_{Al}$ shear-planes, and the difference is negligible in both ADF STEM and HRTEM. This is mainly because the sheared precipitates were created by rigid translations without relaxation due to a lack of suitable molecular dynamics potentials. However, it is unlikely that the shearing planes themselves are the main source of ADF STEM and HRTEM contrast, because of their relatively small volume compared to the full specimen volume. In addition, as the next section will show, much of the contrast in experimental images can be explained by the through-thickness position of the first shearing plane, and the total number of shearing planes. We therefore focus on different Burgers vectors here.

Figure 4 shows how some slip systems appear in ADF STEM and HRTEM images. Different Burgers vectors have a major impact on HRTEM and ADF STEM contrast. The bands of weak Fourier components in HRTEM FFT power spectra are perpendicular to the active Burgers vector, and the superposition of atomic columns in ADF STEM images also changes for

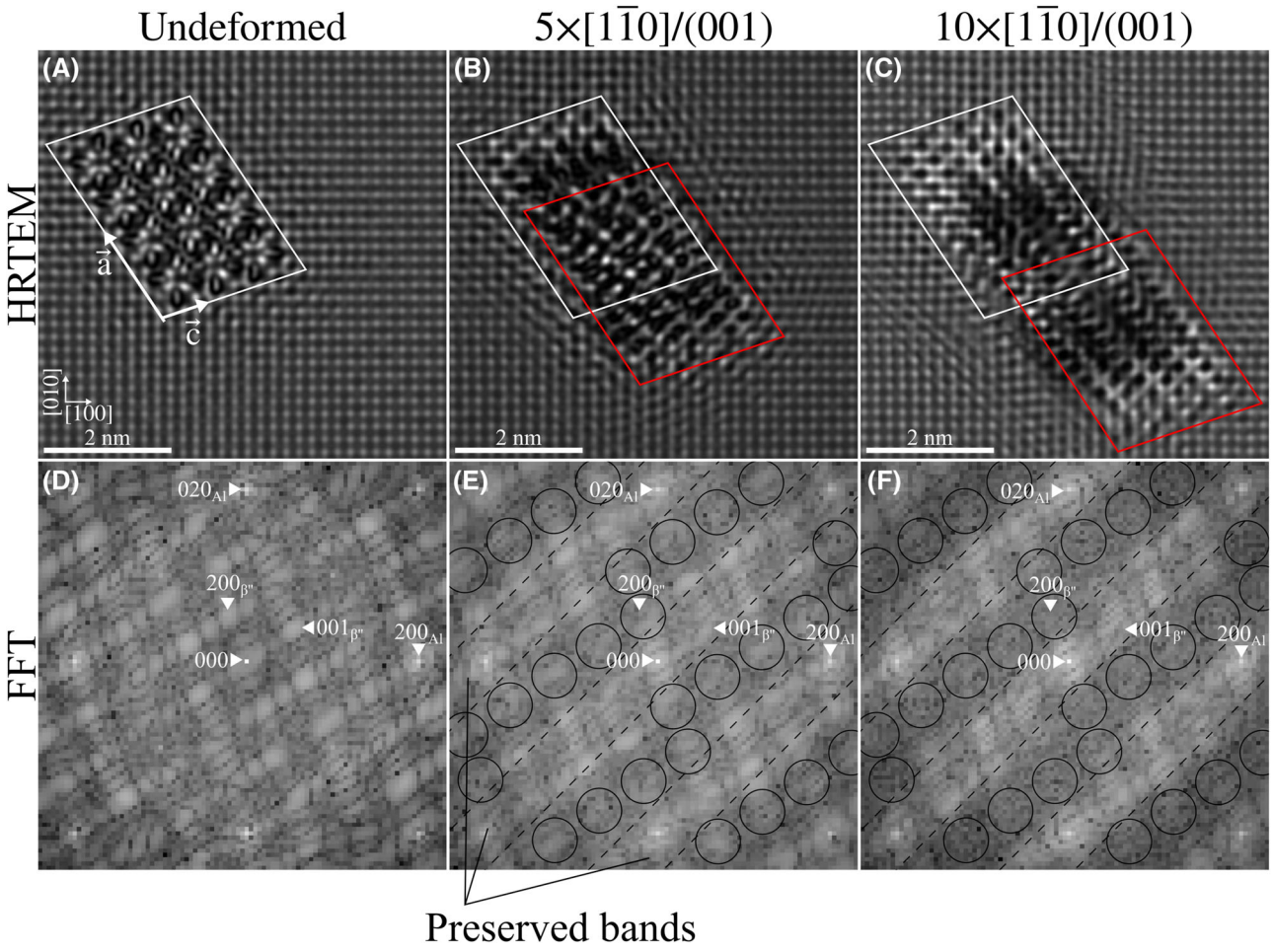

Fig. 3. Simulated HRTEM images of β'' precipitates in an aluminium matrix with different number of shear-planes distributed through the thickness. (A) shows the HRTEM image of a model with no shear-planes, whereas (B) and (C) show models with shearing planes at $z = 14, 31.5, 48.5, 65.5, 83$ and $z = 6.5, 15.5, 25, 34.5, 44, 53, 62.5, 72, 81.5, 90.5$ unit cells below the specimen surface, respectively. The initial and last segment positions are indicated by the white and red boxes, respectively. FFT power spectra are given for each HRTEM image in (D)–(F). Circles in (E) and (F) mark reduced Fourier components, whereas the dashed lines mark bands of preserved Fourier components.

different Burgers vectors. Weak elements of the β'' unit cell, called a β'' 'eye' can be seen in precipitates sheared by $\frac{1}{2}[\bar{1}0\bar{1}]_{Al}$, but the contrast is overall poor. Burgers vectors with $\frac{1}{2}[\bar{1}\bar{1}0]_{Al}$ produces even poorer contrast, and the β'' unit cell can hardly be recognized at all. On the other hand, $\frac{1}{2}[1\bar{1}0]_{Al}$ Burgers vectors produce what appears like a superposition of images from the first and second precipitate segments, as shown previously in Figure 2. The contrast is a little weaker with 10 shear-planes than with a single shear-plane, which is probably because of reduced channelling through the thickness when there are several shear-planes. Nevertheless, the superposition of the first and second segment indicates that the atomic columns of a precipitate sheared along $[1\bar{1}0]$ allow for better channelling conditions. The reason why different Burgers vectors produce such different ADF STEM image contrasts is seen from Table 1. A $\frac{1}{2}[1\bar{1}0]_{Al}$ Burgers vector corresponds to a shift of $[\frac{-1}{6}0\frac{1}{12}]_{\beta''}$, i.e. along $[\bar{2}01]_{\beta''}$ which is a relatively high symmetry direction. A $\frac{1}{2}[\bar{1}\bar{1}0]_{Al}$ Burgers vector, however, corresponds to a shift along $[\frac{-1}{11}0\frac{-1}{2}]_{\beta''} \approx [\bar{1}0\bar{6}]_{\beta''}$, which is a direction with less symmetry.

Comparison with experimental data. Figure 5 presents some experimental ADF STEM images from undeformed and 20% compressed specimens of the Al-Mg-Si alloy AA6060 in peak-hardness condition where most precipitates are of the β'' phase taken from Christiansen *et al.* (2019a). Precipitates in the deformed state can either appear like precipitates in undeformed specimens, with sharp β'' unit cells in parts of the cross-section (Fig. 5B), or with contrast features such as the one shown in Figure 5C. The fact that precipitates in the same specimen can appear either sharp or like the one in Figure 5C can be explained from the position of the shear-plane closest to the specimen surface. In particular, the similarity between the simulation in, for example, Figure 2D and the magnified

© 2020 The Authors. *Journal of Microscopy* published by John Wiley & Sons Ltd on behalf of Royal Microscopical Society,

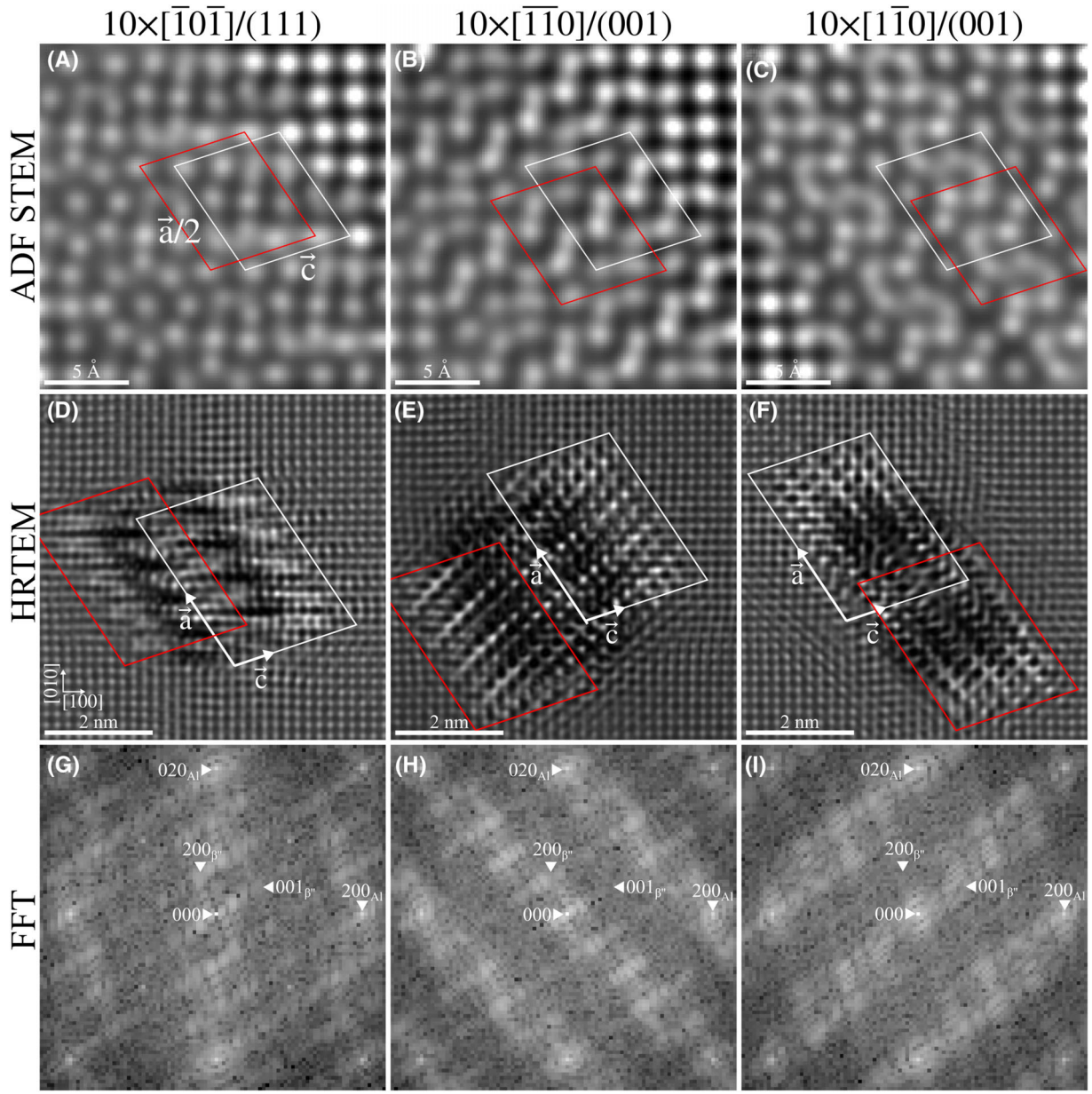

Fig. 4. The effect of slip systems on ADF STEM (A–C) and HRTEM (D–F) images of sheared β'' precipitates in an aluminium matrix. FFT power spectra of the HRTEM images are given in (G)–(I). Each column refers to the $[\bar{1}0\bar{1}]/(111)$, $[\bar{1}\bar{1}0]/(001)$ or $[1\bar{1}0]/(001)$ slip systems. White and red boxes indicate the first and last precipitate unit cells (for ADF STEM) or cross-section outlines (for HRTEM), respectively. For ADF STEM, the vertices of the boxes correspond to centres of β'' 'eyes'.

region in Figure 5C indicates that a shear-plane with Burgers vector $[1\bar{1}0]_{Al}$ lies close to the specimen surface in Figure 5C. The more blurry region of Figure 5C and the blurry regions in Figure 5B, on the other hand, are not likely to be reproduced by simulations because of the many different possible shearing configurations in real specimens. With several active slip systems producing different atomic configurations of precipitates, the number of possible shear configurations is very high and it is highly unlikely that exact configurations can be determined from combining experiments and image simulations. Nevertheless, it is important to realize that even for such complex configurations, the shear planes must be relatively close to the specimen surface to be visible in ADF STEM. For the precipitate imaged in Figure 5C for example, the different contrast regions might be explained by an inclined shear-plane very close to the specimen surface rather than a parallel one.

Because many precipitates in deformed specimens exhibit some sort of modified ADF STEM contrast experimentally, the

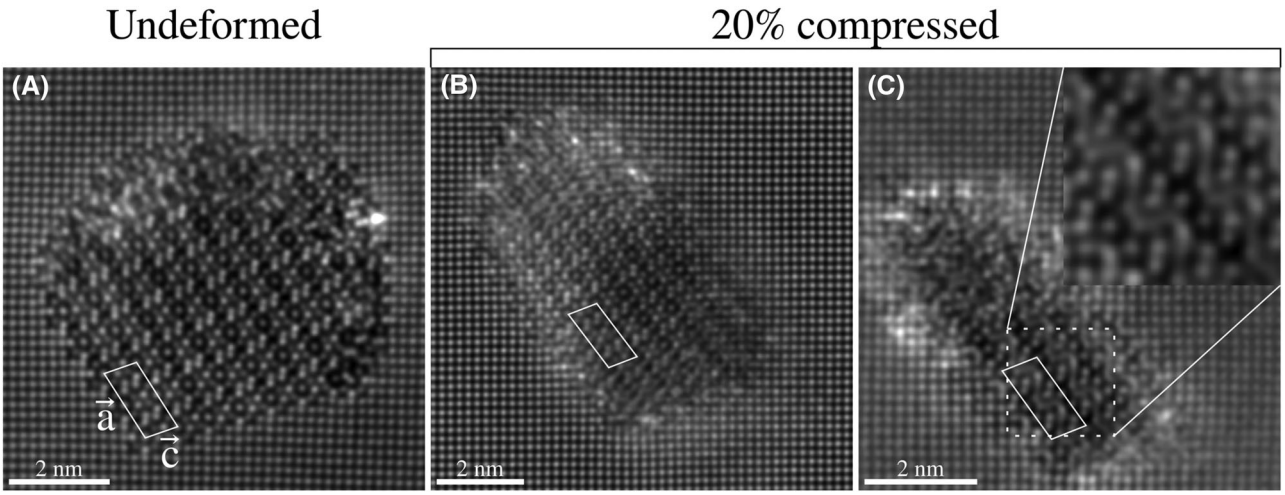

Fig. 5. Experimental ADF STEM images in undeformed (A) and in 20% compressed (B, C) specimens acquired on an aberration corrected JEOL ARM200F (convergence semiangle $\alpha = 27$ mrad, collection semiangles 48–206 mrad, acceleration voltage 200 kV, and spherical aberration $C_3 \approx -300$ nm) from Christiansen *et al.* (2019a). The images are through-stack averages of nonrigidly aligned images in a stack of fast acquisitions (SmartAlign; Jones *et al.* (2015)) and have been Gaussian-filtered (full-width at half maximum 1 Å) to remove noise.

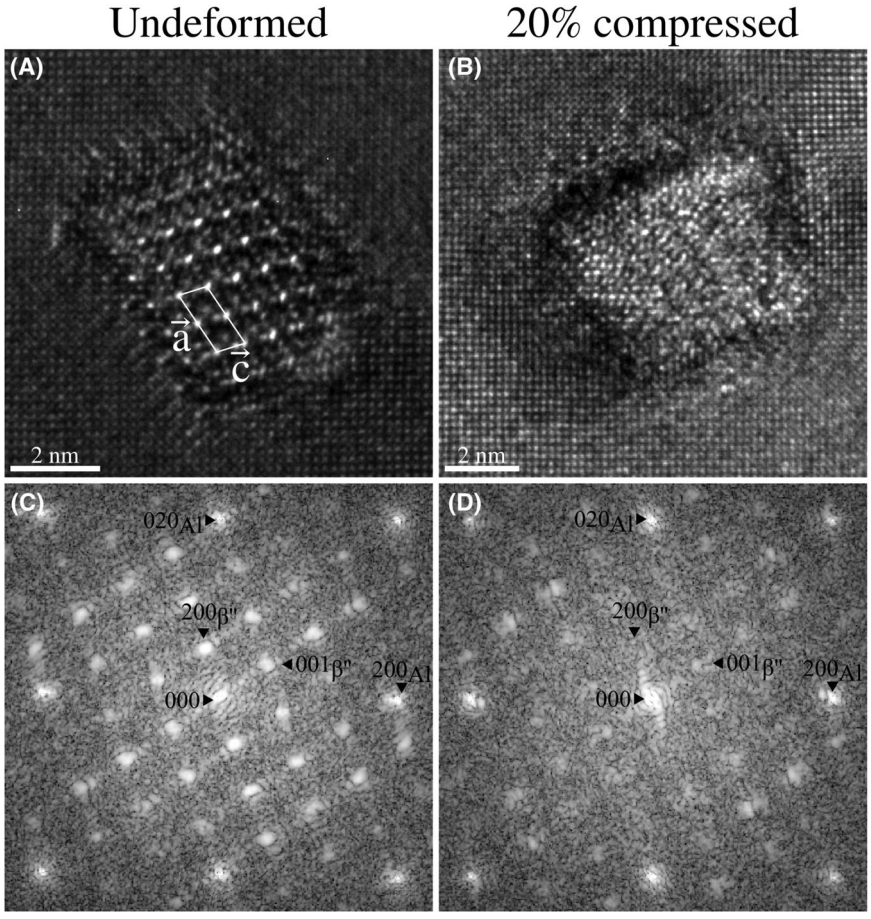

Fig. 6. Experimental HRTEM images of β'' precipitates in an aluminium matrix and corresponding FFT power spectra in undeformed (A, C) and in 20% compressed (B, D) specimens acquired on a JEOL JEM2100F (acceleration voltage 200 kV, and spherical aberration $C_3 \approx 1$ mm) from Christiansen *et al.* (2019a).

© 2020 The Authors. *Journal of Microscopy* published by John Wiley & Sons Ltd on behalf of Royal Microscopical Society,

probability of finding a shear-plane close to the specimen surface is relatively high. Because this probability increases with the number of shear-planes (and inversely with the segment lengths), this modified contrast also indicates that precipitates in Christiansen *et al.* (2019b) are sheared relatively many times and that the shear-planes are distributed through the thickness. This also agrees with the experimental HRTEM image shown in Figure 6. In this figure, Fourier components in the FFT power spectra are weaker in the deformed specimen compared to the undeformed specimen. Although it is challenging to directly compare FFT power spectra of the simulations and the experiments (as a result of the choice of apodization in the experimental image for example), the experimental power spectrum in Figure 6D seems to exhibit the same weak bands of Fourier components as the simulations in, for example, Figure 4I. Hence, the experimental HRTEM images of deformed specimens are also in agreement with precipitates sheared several times.

An interesting point is that the bands in Figure 6D are perpendicular to $[1\bar{1}0]_{\mathrm{Al}}$, which indicates that this is the most active Burgers vector for this precipitate. The ADF STEM image in Figure 5C is from a different precipitate, but also indicates that the most active Burgers vector is $[1\bar{1}0]_{\mathrm{Al}}$. Whether it is purely coincidental that two different precipitates appear to be sheared by the same Burgers vector remains to be investigated, but it might indicate a preferential Burgers vector for shearing β'' precipitates. In the future, it might be possible to determine whether precipitates of a given orientation are more likely to be sheared by some Burgers vectors than others (the other Burgers vectors might instead result in a looping process for instance) and thus provide valuable insight into the shearing process of β'' precipitates.

Conclusions

Shear-planes in β'' precipitates are detectable by ADF STEM if they lie $\sim$ 6–18 unit cells from the specimen surface. A certain number of shear-planes >5 are also needed to produce notable effects in HRTEM images. Compared with experimental data, these results indicate that β'' precipitates are sheared several times at different locations along their lengths. Different Burgers vectors produce different contrast features in both ADF STEM and HRTEM, as long as the previous conditions are met, whereas (111) and (001) slip planes cannot be distinguished.

Acknowledgements

The authors gratefully acknowledge the Research Council of Norway for funding through the SFI CASA project (grant number 237885), the NORTEM infrastructure project (grant number 197405), the research project Mind The Gap (grant number 231762) and the Sigma2 high performance computing clusters (grant numbers 269905/NN9158K). The IDUN cluster at NTNU HPC Group is also gratefully acknowledged for the use of computing capabilities.

Conflict of interest

The authors declare no conflict of interest.

Data availability

Many of the simulation results produced for this work are openly available from he Zenodo data archive repository at https://doi.org/10.5281/zenodo.3694308 Christiansen *et al.* (2020).

References

Andersen, S.J., Zandbergen, H.W., Jansen, J., Træholt, C., Tundal, U. & Reiso, O. (1998) The crystal structure of the β'' phase in Al-Si alloys. *Acta Materialia* **46**, 3283–3298. https://doi.org/10.1016/S1359-6454(97)00493-X.

Ardell, A.J. (1985) Precipitation hardening. *Metallographical Transactions A* **16**, 2131–2165. https://doi.org/10.1007/BF02670416.

Christiansen, E., Marioara, C.D., Holmedal, B., Hopperstad, O.S. & Holmestad, R. (2019a). Data for 'Nano-scale characterisation of sheared β'' precipitates in a deformed Al-Mg-Si alloy'. Zenodo, V1. https://doi.org/10.5281/zenodo.2652906.

Christiansen, E., Marioara, C.D., Holmedal, B., Hopperstad, O.S. & Holmestad, R. (2019b) Nano-scale characterisation of sheared β'' precipitates in a deformed Al-Mg-Si alloy. *Scientific Reports* **9**. https://doi.org/10.1038/s41598-019-53772-4.

Christiansen, E., Ringdalen, I.G., Bjørge, R., Marioara, C.D. & Holmestad, R. (2020). Simulated STEM and HRTEM images of sheared β''precipitates. Zenodo, V1. https://doi.org/10.5281/zenodo.3694308.

Cowley, J.M. & Moodie, A.F. (1957) The scattering of electrons by atoms and crystals. I. A new theoretical approach. *Acta Crystallographica* **10**, 609–619. https://doi.org/10.1107/S0365110X57002194.

de la Peña, F., Prestat, E., Fauske, V.T. *et al.* (2019) hyperspy/hyperspy: Hyperspy v1.5.2. https://doi.org/10.5281/zenodo.3396791.

Edwards, G.A., Stiller, K., Dunlop, G.L. & Couper, M.J. (1998) The precipitation sequence in Al-Si alloys. *Acta Materialia* **46**, 3893–3904. https://doi.org/10.1016/S1359-6454(98)00059-7.

Hillyard, S., Loane, R.F. & Silcox, J. (1993) Annular dark-field imaging: resolution and thickness effects. *Ultramicroscopy* **49**, 14–25. https://doi.org/10.1016/0304-3991(93)90209-G.

Hillyard, S. & Silcox, J. (1993) Thickness effects in ADF STEM zone axis images. *Ultramicroscopy* **52**, 325–334. https://doi.org/10.1016/0304-3991(93)90043-W.

Hyvärinen, A. & Oja, E. (2000) Independent component analysis: algorithms and applications. *Neural Networks* **13**, 411–430. https://doi.org/10.1016/S0893-6080(00)00026-5.

Jones, L., Yang, H., Pennycook, T.J., Marshall, M.S.J., Van Aert, S., Browning, N.D., Castell, M.R. & Nellist, P.D. (2015) Smart Align–a new tool for robust non-rigid registration of scanning microscope data. *Advanced Structural and Chemical Imaging* **1**. http://doi.org/10.1186/s40679-015-0008-4

Klenov, D.O. & Stemmer, S. (2006) Contributions to the contrast in experimental high-angle annular dark-field images. *Ultramicroscopy* **106**, 889–901. https://doi.org/10.1016/j.ultramic.2006.03.007.

Liu, X.-Y. & Adams, J. (1998) Grain-boundary segregation in Al–10%Mg alloys at hot working temperatures. *Acta Materialia* **46**, 3467–3476. https://doi.org/10.1016/S1359-6454(98)00038-X.

Lobato, I., Van Aert, S. & Verbeeck, J. (2016) Progress and new advances in simulating electron microscopy datasets using multem. *Ultramicroscopy* **168**, 17–27. https://doi.org/10.1016/j.ultramic.2016.06.003.

Lobato, I. & Van Dyck, D. (2014) An accurate parameterization for the scattering factors, electron densities and electrostatic potentials for neutral atoms that obey all physical constraints. *Acta Crystallographica A* **70**, 636–649. https://doi.org/10.1107/S205327331401643X.

Lobato, I. & Van Dyck, D. (2015) MULTEM: A new multislice program to perform accurate and fast electron diffraction and imaging simulations using Graphics Processing Units with CUDA. *Ultramicroscopy* **156**, 9–17. https://doi.org/10.1016/j.ultramic.2015.04.016.

Martinez, G.T., van den Bos, K. H.W., Alania, M., Nellist, P.D. & Van Aert, S. (2018) Thickness dependence of scattering cross-sections in quantitative scanning transmission electron microscopy. *Ultramicroscopy* **187**, 84–92. https://doi.org/10.1016/j.ultramic.2018.01.005.

Misumi, K., Kaneko, K., Nishiyama, T. *et al.* (2014) Three-dimensional characterization of interaction between β'' precipitate and dislocation in Al-Si alloy. *Journal of Alloys and Compounds* **600**, 29–33. https://doi.org/10.1016/j.jallcom.2014.02.059.

Ninive, P.H., Strandlie, A., Gulbrandsen-Dahl, S. *et al.* (2014) Detailed atomistic insight into the β'' phase in Al-Si alloys. *Acta Materialia* **69**, 126–134. https://doi.org/10.1016/j.actamat.2014.01.052.

Peng, L.-M., Ren, G., Dudarev, S.L. & Whelan, M.J. (1996) Debye–Waller factors and absorptive scattering factors of elemental crystals. *Acta Crystallographica A* **52**, 456–470. https://doi.org/10.1107/S010876739600089X.

Pennycook, S. & Jesson, D. (1991) High-resolution Z-contrast imaging of crystals. *Ultramicroscopy* **37**, 14–38. https://doi.org/10.1016/0304-3991(91)90004-P.

Plimpton, S. (1995) Fast parallel algorithms for short-range molecular dynamics. *Journal of Computational Physics* **117**, 1–19. https://doi.org/10.1006/jcph.1995.1039.

Poole, W.J., Wang, X., Lloyd, D.J. & Embury, J.D. (2005) The shearable-non-shearable transition in Al-Mg-Si-Cu precipitation hardening alloys: implications on the distribution of slip, work hardening and fracture. *Philosophical Magazine* **85**, 3113–3135. https://doi.org/10.1080/14786430500154935.

Saito, T., Mørtsell, E.A., Wenner, S., Marioara, C.D., Andersen, S.J., Friis, J., Matsuda, K. & Holmestad, R. (2018) Atomic structures of precipitates in Al-Mg-Si alloys with small additions of other elements. *Advanced Engineering Materials* **20**, 1800125. https://doi.org/10.1002/adem.201800125.

Maunders, C., Dwyer, C., Tiemeijer, P.C. & Etheridge, J. (2011) Practical methods for the measurement of spatial coherence—a comparative study. *Ultramicroscopy* **111**, 1437–1446. https://doi.org/10.1016/j.ultramic.2011.05.011.

Kirkland, Earl J. *Advanced Computing in Electron Microscopy* (Springer, Boston, 2010), 2 edn. https://doi.org/10.1007/978-1-4419-6533-2.

Själander, M., Jahre, M., Tufte, G. & Reissmann, N. (2019) Epic: an energy-efficient, high-performance GPGPU computing research infrastructure. arXiv:1912.05848 [cs.DC]. https://arxiv.org/abs/1912.05848v1.

Stukowski, A. (2010) Visualization and analysis of atomistic simulation data with OVITO: the open visualization tool. *Modelling and Simulation in Materials Science and Engineering* **18**, 015012. https://doi.org/10.1088/0965-0393/18/1/015012.

Van Aert, S., Geuens, P., Van Dyck, D., Kisielowski, C. & Jinschek, J. (2007) Electron channelling based crystallography. *Ultramicroscopy* **107**, 551–558. http://doi.org/10.1016/j.ultramic.2006.04.031.

Van Dyck, D. & Chen, J.H. (1999) Towards an exit wave in closed analytical form. *Acta Crystallographica A* **55**, 212–215. https://doi.org/10.1107/S0108767398011337.

Xu, Q., Van Dyck, D. & Zandbergen, H.W. (2010) From thickness dependent exit waves to projected potential: thickness derivative approach. *Ultramicroscopy* **110**, 535–542. https://doi.org/10.1016/j.ultramic.2009.10.008.

Zhou, T. & Tao, D. (2011) GoDec: Randomized lowrank & sparse matrix decomposition in noisy case. L. Getoor & T. Scheffer, In *Proceedings of the 28th International Conference on Machine Learning ICML '11*, (pp. 33–40). http://www.icml-2011.org/papers/41_icmlpaper.pdf.

© 2020 The Authors. *Journal of Microscopy* published by John Wiley & Sons Ltd on behalf of Royal Microscopical Society, **00**, 1–9